J. Fluid Mech. (2025), *vol.* 1017, A41, doi:10.1017/jfm.2025.10421

Orientation of flat bodies of revolution in shear flows at low Reynolds number

Davide Di Giusto[1,2], **Laurence Bergougnoux**[1] **and Elisabeth Guazzelli**[3]

[1]Aix Marseille Université, CNRS, IUSTI, Marseille, France

[2]Dipartimento Politecnico di Ingegneria e Architettura, University of Udine, Italy

[3]Université Paris Cité, CNRS, Matière et Systèmes Complexes UMR 7057, Paris, France

Corresponding author: Davide Di Giusto, digiusto.davide@spes.uniud.it

(Received 4 December 2024; revised 28 March 2025; accepted 28 April 2025)

We experimentally investigate the rotational dynamics of neutrally buoyant flat bodies of revolution (spheroids, disks and rings with different cross-sectional shapes) in shear flows. In the Stokes regime, the axis of revolution of these rigid particles moves in one of a family of closed periodic Jeffery orbits. Inertia is able to lift the orbit degeneracy and induces drift among several rotations towards limiting stable orbits. Furthermore, permanent alignment can be achieved for disks and rings with triangular cross-sectional shapes, provided the inertia is sufficiently high. The bifurcations between the different dynamics are compared with those predicted by small-inertia asymptotic theories and numerical simulations.

Key words: suspensions, slender-body theory, particle/fluid flow

---

1. Introduction

In the absence of inertial and Brownian effects, the axis of revolution of an axisymmetric rigid particle suspended in a simple shear flow rotates along one of an infinite family of closed periodic orbits, known as Jeffery orbits. These orbits depend solely on the initial orientation of the particle. This result was demonstrated by Jeffery (1922) for ellipsoids of revolution (or spheroids) and extended to almost any body of revolution by Bretherton (1962) as long as an effective aspect ratio r_e is used in the equation for the rotation rate in lieu of the actual aspect ratio r. For a simple shear flow with a shear rate of $\dot{\gamma}$, the Jeffery period of rotation of the body is given by $T_J = 2\pi(r_e + 1/r_e)/\dot{\gamma}$, where $r_e \neq r$ in general, except for a spheroid for which $r_e = r$.

The question of whether particles of specific shapes can stop rotating and achieve a permanent alignment was first raised by Bretherton (1962). Bretherton (1962) suggested that a slender dumbbell consisting of two asymmetrical beads connected by a long rigid rod could stop rotating, but concluded that this body was too unrealistically thin to be constructed. The issue was recently revivified by Singh, Koch & Stroock (2013) and Borker, Stroock & Koch (2018). Singh *et al.* (2013) showed that rings with appropriate asymmetric cross-sectional shapes (i.e. a thinner outer edge and thicker inner edge) could align permanently. The asymmetry between the inner and outer portions of the ring cross-section was shown to result in a torque capable of cancelling the torque attempting to rotate the particle in the vorticity direction. Borker *et al.* (2018) further expanded this analysis by considering rings with a cross-section having a blunt inner and sharper outer edge, such as Y-, L-, T- and triangular-shaped cross-sections, which could align at smaller aspect ratios ($\lesssim 1/10$) than the minimum aspect ratio of 1/30 reported by Singh *et al.* (2013). The question of whether such particles can be designed in practice and observed to align in the Stokes regime remains open.

Inertia is capable of modifying the rotational dynamics of axisymmetric rigid particles. Weak inertia is indeed capable of lifting the degeneracy of the infinitely many stable Jeffery orbits and inducing drift among several rotations towards limiting stable orbits. Prolate bodies are attracted towards the tumbling orbit, while oblate bodies are carried towards the spinning or the tumbling orbit as demonstrated in theoretical (Subramanian & Koch 2005, 2006; Einarsson *et al.* 2015*a*,*b*; Dabade, Marath & Subramanian 2016; Marath & Subramanian 2017, 2018) and numerical (Rosén *et al.* 2015*a*) works but also experiments (Di Giusto *et al.* 2024). In the latter case of oblate bodies, a bifurcation between stable and unstable tumbling is predicted at an aspect ratio ≈ 0.14 by asymptotic theories (Einarsson *et al.* 2015*b*; Dabade *et al.* 2016) and is shown to survive up to particle Reynolds numbers of the order of 5 in simulations (Rosén *et al.* 2015*a*). However, this bifurcation is unexpectedly not observed experimentally (Di Giusto *et al.* 2024). As inertia is further increased, the period of rotation increases and a bifurcation towards a stable fixed orientation is predicted (Ding & Aidun 2000). As demonstrated by Ding & Aidun (2000), for an elliptical cylinder or an ellipsoid suspended in shear flow, the transition to stable orientation occurs through a saddle-node bifurcation, resulting in a period of rotation that varies as a power-law of the distance to the transition with an exponent of –1/2 when approaching the transition. This later scaling law was validated in an experimental study of an elliptical cylinder subjected to shear flow (Zettner & Yoda 2001). Further research delved more deeply into the complete dynamical states of particles in shear flow with inertia (Rosén *et al.* 2014, 2015*a,b*). In particular, it was demonstrated that the exponent $-1/2$ in the scaling law is universal and independent of particle shape or any geometric aspect ratio in the flow (Rosén *et al.* 2014).

The present work is an experimental investigation of the rotational dynamics of neutrally buoyant flat bodies of revolution (oblate spheroids, disks, rings with different cross-sectional shapes) in shear flows. The objective is to determine whether a bifurcation towards stable orientation can be observed. The experimental methods are described in § 2. Deep learning methods are used to infer the three-dimensional orientation of the bodies. The experimental results are presented in § 3. The bifurcations between the different dynamics are compared with those predicted by asymptotic theories and numerical simulations. Concluding remarks are drawn in § 4.

2. Experimental methods

2.1. *Particles and fluids*

This study considers oblate particles of various shapes, some of which are displayed in figure 1. These include axisymmetric bodies such as spheroids, disks and rings, classified

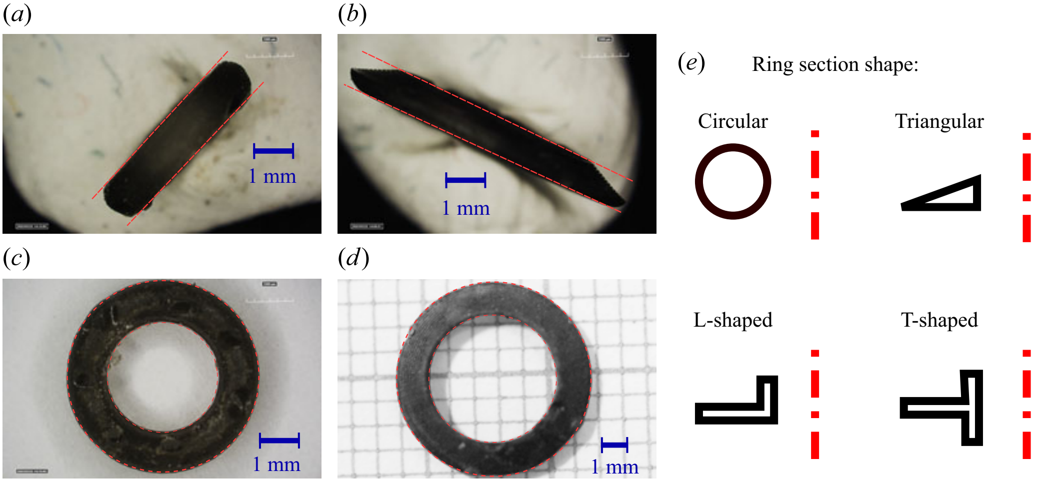

Figure 1. Typical particles used in the experiments: (*a*) side and (*c*) top views of the circular ring R02; (*b*) side and (*d*) top views of the triangular ring TR012. (*e*) Illustration of the four different ring sections considered in this study. The particle symmetry axis is drawn as a dash-dotted line for each case.

based on their particle aspect ratio r, defined as the ratio between their length 2ℓ and their diameter $2a$. A variety of rings with differing cross-sectional shapes are manufactured, including those with circular, triangular, L-shaped and T-shaped cross-sections. The shape of these rings is contingent upon a third parameter, namely the radius of the inner hole, which is denoted as b. Images of the particles are captured with a Hirox RH-2000 digital microscope, which offers a resolution of more than 200 pixels per mm. Ten digital measurements of the particle sizes are then performed using the software ImageJ, and the statistical analysis of the results is reported in table 1.

Particles are digitally designed using Blender Community (2018) and fabricated by three different rapid prototyping methods. The first batch (batch I) is constituted by disks (D002, D003, D004) that have been laser cut from rigid Plexiglas sheets with a density of 1160 $\mathrm{kg\,m^{-3}}$. Stereolithography is employed to manufacture the particles constituting the second batch (batch II), which includes one ellipsoid (ELL06), all circular rings, the less flat triangular rings (TR01, TR012, TR04), and the special L-shaped (RL01) and T-shaped (RT01) rings. This method is based on the polymerisation of a UV-sensitive resin over three-dimensional layers, resulting in the production of high-resolution objects (with a resolution of 25 μm) with an estimated density of 1200 $\mathrm{kg\,m^{-3}}$. The third and final batch (batch III) comprises the most slender triangular rings (TR003, TR005, TR008), which were fabricated using a computer numerical control (CNC) three-dimensional (3-D) milling machine on thin sheets of Plexiglas. All the selected materials possess a Young modulus of a few gigaPascals, which is sufficient to resist deformation within the viscous shear flow, even for the thinnest sections (TR003).

In our experiments, it is necessary to suspend a single particle at a time in a viscous shear flow under neutrally buoyant conditions. To achieve this, citric acid and Ucon oil are mixed with pure water to prepare the necessary density-matched fluid. A variable quantity of Ucon oil is added to the solution to adjust its viscosity within the range of $0.02 \leqslant \mu \leqslant 0.8$ Pa s. Thereafter, the concentration of citric acid is incrementally increased until the density of the fluid ρ_f matches that of the considered particle ρ_p. The final density of the fluid is determined by means of an Anton Paar densimeter, with an estimated uncertainty of 4 $\mathrm{kg\,m^{-3}}$. Rheological measurements are employed to ascertain the viscosity of the solution, with an uncertainty below 0.01 Pa s.

Name	Shape	r	a (mm)	ℓ (mm)	b (mm)	κ	Batch
D002	Disk	0.026 ± 0.005	4.790 ± 0.033	0.125 ± 0.025	–	0.355 ± 0.013	I
D003	Disk	0.032 ± 0.006	7.732 ± 0.031	0.250 ± 0.050	–	0.573 ± 0.021	I
D004	Disk	0.044 ± 0.009	5.699 ± 0.047	0.250 ± 0.050	–	0.422 ± 0.016	I
ELL06	Spheroid	0.561 ± 0.002	2.291 ± 0.009	1.286 ± 0.002	–	0.170 ± 0.006	II
R009	Circular ring	0.087 ± 0.012	8.220 ± 0.024	0.715 ± 0.099	–	0.609 ± 0.023	II
R01	Circular ring	0.132 ± 0.012	8.054 ± 0.074	1.064 ± 0.094	–	0.597 ± 0.023	II
R02	Circular ring	0.227 ± 0.008	4.999 ± 0.009	1.135 ± 0.039	–	0.370 ± 0.014	II
R05	Circular ring	0.452 ± 0.073	5.013 ± 0.015	2.267 ± 0.367	–	0.371 ± 0.014	II
TR003	Triangular ring	0.031 ± 0.004	8.130 ± 0.095	0.256 ± 0.029	6.244 ± 0.042	0.602 ± 0.023	III
TR005	Triangular ring	0.053 ± 0.002	6.478 ± 0.063	0.343 ± 0.015	5.563 ± 0.064	0.480 ± 0.018	III
TR008	Triangular ring	0.085 ± 0.003	10.122 ± 0.029	0.864 ± 0.034	2.262 ± 0.037	0.750 ± 0.028	III
TR01	Triangular ring	0.109 ± 0.006	9.685 ± 0.312	1.058 ± 0.049	2.820 ± 0.394	0.717 ± 0.035	II
TR012	Triangular ring	0.120 ± 0.007	7.947 ± 0.025	0.954 ± 0.059	2.787 ± 0.046	0.589 ± 0.022	II
TR04	Triangular ring	0.397 ± 0.002	7.760 ± 0.020	3.080 ± 0.010	3.630 ± 0.050	0.575 ± 0.021	II
RL01	L-shaped ring	0.097 ± 0.002	10.33 ± 0.05	1.01 ± 0.02	2.66 ± 0.06	0.77 ± 0.03	II
RT01	T-shaped ring	0.116 ± 0.004	5.152 ± 0.014	0.596 ± 0.018	1.349 ± 0.026	0.382 ± 0.014	II

Table 1. Characteristics of all the particles used in the experiments. The columns from left to right provide the following information: code name, shape, mean aspect ratio r, radius a, half-length ℓ, hole radius b, confinement ratio κ and identification of the production method.

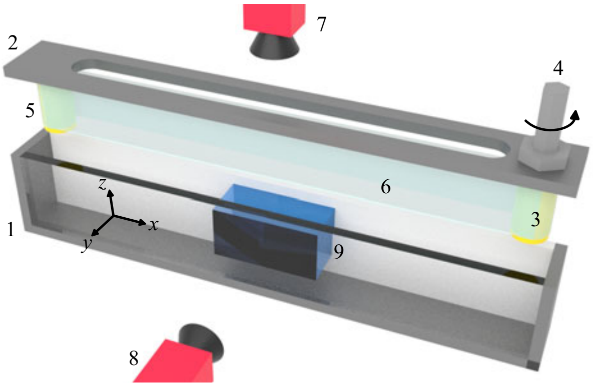

Figure 2. Sketch of the experimental apparatus. The tank (1) is shown with its perforated lid (2), through which the two cylinders are hanging on both ends. The first cylinder is free to rotate (3), being coupled to a transmission shaft (4) through a rolling bearing. The second cylinder is fixed (5). Between them, a transparent plastic belt made of Mylar is kept under tension (6). The two cameras are also depicted: one is oriented to observe the flow-gradient (x, y) plane (7), while the other is focused on the flow-vorticity (x, z) plane (8). The operative volume where the experiments are performed is also shown in blue (9).

2.2. *Shearing cell*

A linear shearing cell apparatus is employed in the experiments, as illustrated in figure 2 and described in detail by Di Giusto *et al.* (2024). The apparatus comprises a small tank (500 mm long, 40 mm wide and 90 mm deep) with transparent walls. A transparent and flexible Mylar film is driven by an electric motor and pulled in tension by two cylinders hanging at the extremities of the cell lid along its long side. During each experiment, approximately 1.2 l of viscous fluid are poured into the tank at a controlled room temperature of $23^\circ \pm 1^\circ$. As the film continuously rotates at a constant velocity, it shears the fluid confined between its inner surfaces, held at a distance L_y of 27 mm.

The sheared particles are inevitably confined between the two sides of the transparent belt, with a confinement ratio $\kappa = 2a/L_y$. Mean values of the confinement ratio are reported in table 1.

The operative volume of the experiments extends for 140 mm in the flow direction x, 30 mm in the vorticity/gravity direction z and 27 mm in the gradient direction y, with the boundaries defined by the two inner surfaces of the transparent film. Two Allied Prosilica GX1910 cameras are positioned to capture this region of the shear cell, as illustrated in figure 2. Both cameras are equipped with a Nikon Micro-Nikkor 55 mm f2.8 objective, which enables the imaging of the shear cell with 1920 × 1080 pixels from a distance of approximately half a metre. This produces undistorted images with a sufficient focal depth and a resolution of approximately 20 pixels per mm over the considered particles. The top camera is aligned with the vorticity axis z and images the flow-gradient (x, y) plane, while the side camera is aligned with the gradient axis y and views the flow-vorticity (x,z) plane. Planar (x, y) particle image velocimetry (PIV) measurements are recorded with the top camera by shedding a laser beam at three different locations along the vorticity axis z, corresponding to the upper, middle and lower sections of the operative volume. This results in the observation of a constant shear rate $\dot{\gamma}$ across the depth of the control volume. A total of 40 PIV measurements is recorded using various viscous fluids, with shear rates linearly varying between $\dot{\gamma} = 3.18 \pm 0.1\ \text{s}^{-1}$ at $\mu = 0.02$ Pa s and $\dot{\gamma} = 3.63 \pm 0.01\ \text{s}^{-1}$ at $\mu = 0.8$ Pa s.

As fluid and particle densities are always matched to prevent sedimentation effects ($\rho_p \simeq \rho_f$), and the fluid is sheared at the highest rate $\dot{\gamma}$ possible, the particle Reynolds number $Re_p = \rho_f a^2 \dot{\gamma}/\mu$ is controlled through the fluid viscosity μ. Hence, inertial effects are produced by reducing the Ucon oil concentration during the preparation of the fluid as it reduces the viscosity μ. This implies that fluid and particle inertia effects are indiscernible ($Re_p = St$, with the Stokes number $St = \rho_p a^2 \dot{\gamma}/\mu$).

2.3. *Measurements*

2.3.1. *Particle tracking*

The experiments are prepared by filling the cell with the selected fluid and initiating the shearing motion of the transparent plastic belt. Subsequently, one particle from those presented in table 1 is selected and positioned at the centre of the operative volume, as close as possible to the zero velocity streamline. In this procedure, the initial orientation of the particle is not precisely controllable and the result is essentially random. At this moment, the video recording by the two cameras is activated and synchronised by a luminous signal, signifying the initiation of the experiment. The frame acquisition is conducted at a rate of 7.5 fps until the particle exits the camera field of view. Experiments are typically repeated between 5 and 10 times for a given particle at each particle Reynolds number, as reported in table 2. This methodology is adequate to measure multiple particle rotations, but does not permit the observation of transverse migration over extended time scales. For this reason, inertial lift measurements are not attempted in this work.

A Python script was developed in-house to track the particle across both top and side camera fields during the recordings of the experiments. The script implements a standard version of the Watershed method calling the high-level functions provided in the OpenCV library (Bradski 2000). In detail, the image is binarised by thresholding to separate between the background and the particle by simple morphological operations. Then, the watershed algorithm is applied to find an accurate estimation of the particle centre in the image plane. This operation is particularly challenging for slender rings,

Particle	$Re_p,\ n_{runs},\ \overline{\Delta t_{run}}/T$				
D002	0.218, 3, 1.16	0.805, 5, 1.17	1.056, 5, 1.45	3.162, 5, –	4.835, 5, –
D003	0.525, 5, 1.01	0.688, 5, 0.89	2.060, 5, –		
D004	0.077, 5, 1.47	1.119, 5, 0.91			
ELL06	0.031, 5, 5.40	0.474, 11, 6.62	0.731, 5, 6.17	1.029, 6, 8.14	
R009	0.098, 5, 2.45	0.869, 5, 1.87			
R01	0.150, 5, 3.47	0.389, 5, 4.55	3.067, 5, 2.35		
R02	0.058, 5, 4.90	0.150, 5, 6.24	1.181, 5, 4.88		
R05	0.058, 5, 4.29	0.151, 5, 6.79	1.188, 5, 2.66		
TR003	0.360, 5, 1.30	0.867, 5, –	1.245, 5, –		
TR005	0.131, 5, 2.35	1.394, 5, –	1.757, 5, –		
TR008	0.149, 5, 2.05	1.069, 5, 1.81	4.898, 5, –		
TR01	0.217, 5, 3.11	0.561, 5, 2.69	4.266, 5, –		
TR012	0.146, 5, 2.79	0.379, 5, 3.11	2.986, 5, 1.61		
TR04	0.084, 5, 3.31	2.097, 5, 3.20			
RL01	0.155, 5, 4.17	1.113, 5, 1.85			
RT01	0.154, 5, 3.44	1.108, 5, 3.70			

Table 2. For each particle type used in the experiments (first column), the particle Reynolds number, Re_p, the number of runs, n_{runs}, and the mean duration of the shearing normalised by the (experimentally measured) mean period of rotation, $\overline{\Delta t_{run}}/T$, are provided. In the case of aligning particles, the mean duration of the shearing is not calculated.

since they offer the lowest surface to the camera field of view. Consequently, each frame is cropped to a $4a \times 4a$ image, which displays the particle under consideration.

2.3.2. *Orientation measurements with convolutional neural network*

The measurement of the orientation of both axisymmetric and asymmetrical particles represents a significant challenge. Cylindrical and ellipsoidal shapes present simple geometrical relations that can be exploited to regress their orientation from their axes-aligned bounding boxes (Di Giusto *et al.* 2024). However, this method is not readily generalisable to asymmetric particle shapes. Consequently, we have developed a new data-driven approach, which is sketched in figure 3.

As previously outlined in § 2.1, the particle fabrication methods necessitate the generation of a digital model of each object in the format of a '.stl' file, see panel (*a*) of figure 3. It is thus possible to create a synthetic dataset of virtual images of oriented particles that closely resemble the frames recorded during the experiments, as illustrated in panel (*b*) of figure 3. Further details regarding the dataset preparation can be found in Appendix A. The labelled data can then be used to train a deep learning model, see panel (*c*) of figure 3, and to measure the particle orientation from pairs of perpendicular views, as detailed in Appendix B. Concurrently, the '.stl' file is used to reproduce a physical copy of the considered particles through rapid prototyping, see panel (*d*) of figure 3, as described in § 2.1. The rotational dynamics of the aforementioned object are then recorded during the experiments, see panel (*e*) of figure 3, using the set-up described in § 2.2.

Two additional operations are conducted during the post-processing of the experimental recordings. First, the Watershed algorithm is applied to track each particle across the

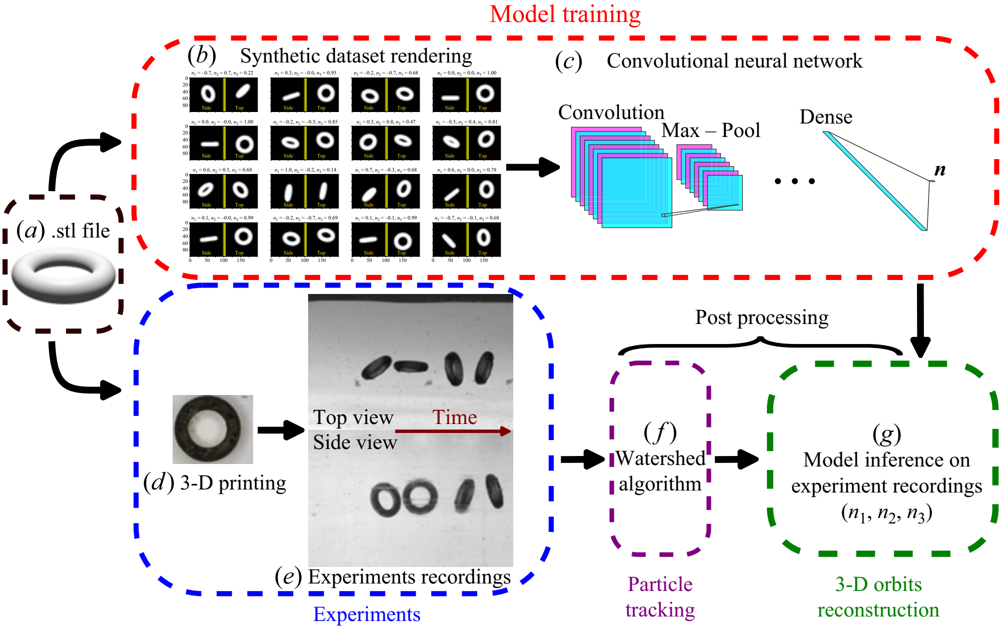

Figure 3. Sketch of the convolutional neural network. The operative process is as follows: a given particle geometry, represented by a '.stl' file in panel (*a*), is used as the basis for the generation of a synthetic data set in Blender in panel (*b*). This data set is then used to train a deep learning model, with the objective of estimating the particle orientation given two perpendicular projections in panel (*c*). A physical particle corresponding to the '.stl' file is also created through rapid prototyping in panel (*d*) and employed in the experiments in panel (*e*). Subsequently, the Watershed method in panel (*f*) is applied to the recorded data from the experiments prior to the deep learning model inference operation in panel (*g*), which estimates the time-evolution of the three-dimensional particle orientation vector $\boldsymbol{n}$ in the given experiment.

camera frames, as described in § 2.3.1. Subsequently, the deep learning model can infer the three-dimensional particle orientation from each couple of perpendicular frames and estimate the rotational dynamics of the considered particles, see panels (*f*) and (*g*) of figure 3.

Among all deep learning architectures, convolutional neural networks (CNNs) are particularly adept at extracting features from visual inputs (Szegedy *et al.* 2015), as evidenced by their successful application to a range of tasks, including face recognition (Taigman *et al.* 2014), real-time object detection (Redmon *et al.* 2016) and autonomous driving (Bojarski *et al.* 2016). CNNs were directly inspired by the hierarchical functioning of neurons in the visual cortex of simple mammals (Hubel & Wiesel 1959, 1968). This resulted in the implementation of a simple convolution down sampling architecture into a first neural network for visual pattern recognition (Fukushima 1980). Subsequently, LeCun *et al.* (1998) stacked convolutional and pooling layers with a fully connected neural network to build the LeNet-5 architecture, one of the first CNNs, and successfully applied it to handwritten digit recognition.

In this study, we adapt the LeNet-5 architecture to quantify the three-dimensional orientation of axisymmetric and asymmetric particles from each pair of perpendicular frames of the video recording of the experiments, as sketched in figure 3. The image pairs are initially processed separately, with each frame of a pair allocated to a dedicated branch comprising three consecutive two-dimensional convolutional layers. These layers have kernel sizes of 5 × 5 pixels, the first layer containing 8 feature maps and the second 16.

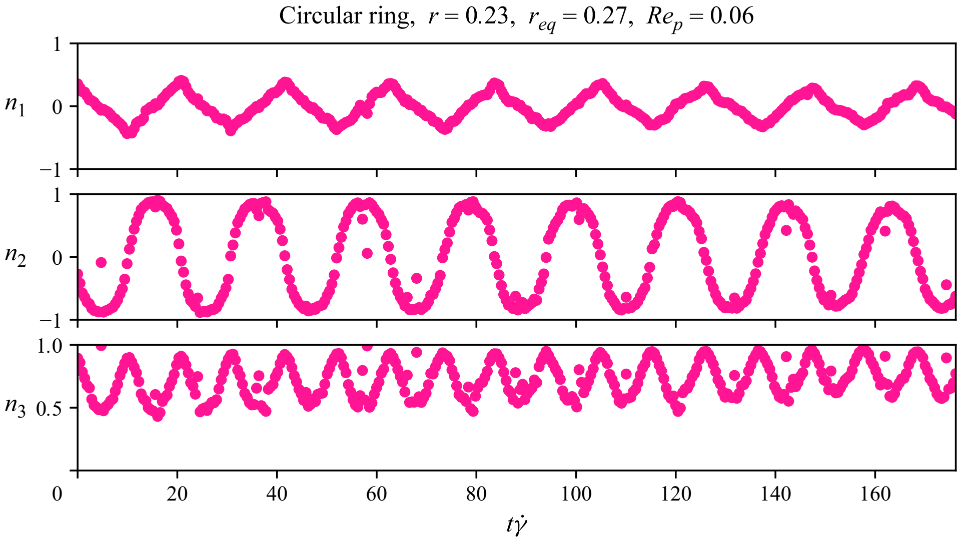

Figure 4. Evolution of the components of the orientation vector $\boldsymbol{n}$, displayed as vertically aligned panels, against the dimensionless time $t\dot{\gamma}$ for the circular ring R02 with aspect ratio $r = 0.23$ at a small $Re_p = 0.06$. See Supplementary movie 1 for animations and the Jupyter Notebook (https://www.cambridge.org/S0022112025104217/JFM-Notebooks/files/figure_4/Figure_4.ipynb) of the figure including the data.

Each convolutional layer is followed by a two-dimensional max-pooling operation with a pool size of 2 × 2 pixels. Subsequently, the two streams are concatenated, and three fully connected layers with 256 features each are applied to ascertain the orientation vector of the particle, represented by $\boldsymbol{n}$. In accordance with Krizhevsky, Sutskever & Hinton (2012), the Rectified Linear Unit (ReLU) was selected as the activation function for all layers except the final one. In this case, a linear mapping was employed to determine the three components of $\boldsymbol{n}$, which were then normalised by their Euclidean norm to ensure the consistency of the orientation. The parameters of the CNN are trained over synthetic images of axisymmetrical and asymmetrical particles generated following the procedure described in Appendix A. The network is trained to infer the particle orientation from its two perpendicular views by minimising a loss function given by the Euclidean norm of the difference between the true particle orientation vector, $\boldsymbol{n}_{true}$, and the predicted particle orientation vector, $\boldsymbol{n}_{pred}$. An additional penalisation is determined whenever a negative value of the n_3 component is observed. The optimisation is performed through the Adam algorithm. Further details about the training procedure can be found in Appendix B.

CNNs have been successfully applied to estimate fluid motion (Cai *et al.* 2019) or to detect submicron particles (Newby *et al.* 2018). However, to the best of our knowledge, this is the first time that such a method has been proposed to measure the orientation of macroscopic axisymmetric and asymmetric particles. Convolutional neural networks (CNNs) are found to provide a satisfactory compromise between simplicity and effectiveness. However, other neural architectures may prove to be more effective. Consequently, a benchmark consisting of a comprehensive set of experimental videos is provided, accompanied by the spheroid ELL06 '.stl' file and training data.

2.3.3. *Data analysis*

Once trained, the neural network is capable of reconstructing the time evolution of the particle orientation vector $\boldsymbol{n}$ during each experiment in a few seconds. A typical result with the circular ring R02 is displayed in figure 4. Despite the presence of occasional noise, the periodic nature of the three components, namely n_1, n_2 and n_3, can be discerned against the dimensionless time $t\dot{\gamma}$. Subsequently, other significant quantities can be determined. The Fourier transform of the signals can be calculated, thereby providing the period, T. Furthermore, a minimum difference threshold criterion is established on the two highest peaks of the power spectrum of the particle polar angles, with the objective of distinguishing between rotational and aligned dynamical states. The components of the reconstructed vector $\boldsymbol{n}$ can be used to determine the azimuthal angle, ϕ, and polar angle, θ, of the orientation. This is achieved by calculating the following expressions:

$$n_1 = \sin(\phi)\sin(\theta), \tag{2.1}$$

$$n_2 = \cos(\phi)\sin(\theta), \tag{2.2}$$

$$n_3 = \cos(\theta). \tag{2.3}$$

The distinction between rotational and aligned dynamical states based on the power spectrum is always visually verified by examining the components of the vector $\boldsymbol{n}$. It is acknowledged that the data may contain some errant points due to minor imprecisions in particle tracking or 3-D orientation estimation. However, the methods used to calculate the period of rotation and to determine the aligned dynamical states are based on Fourier analysis, which results in robustness to these small inaccuracies. Further details can be found in Di Giusto *et al.* (2024).

3. Experimental results

3.1. *Period of rotation*

Figure 5 depicts the dimensionless period of rotation, $T\dot{\gamma}/2\pi$, of the flat bodies of revolution as a function of particle aspect ratio, r. The data are obtained by averaging over all available experiments for small particle Reynolds number, $Re_p \lesssim 0.5$. The measured period of these particles consistently falls below the Jeffery curve, indicating that the period is consistently smaller than that of the corresponding spheroid at the same r. As previously stated in § 1, an equivalent aspect ratio, r_{eq}, can be determined for any body of revolution to recover the Jeffery period. To be more precise, r_{eq} can be calculated from the equation $T\dot{\gamma} = 2\pi(r_{eq} + 1/r_{eq})$, where T represents the measured period of rotation. When the ring has a circular-shaped cross-section, i.e. when the ring is a circular torus, Singh *et al.* (2013) proposed that the effective aspect ratio at the leading order is given by $r_{eq} = 0.903r\sqrt{\ln 1/r}$. This theoretical prediction is in excellent agreement with the present measurements for rings with circular-shaped cross-section, and even for rings with triangular-shaped and L-shaped cross-section. The period of the other bodies (rings with T-shaped cross-section, oblate ellipsoids and disks) appears to be more closely in agreement with the empirical correlation proposed by Harris & Pittman (1975), namely $r_{eq} = 1.14\, r/r^{0.156}$. It is important to highlight that all these particles have always been observed to rotate for $Re_p \lesssim 0.5$. It is possible that the rings may lack the requisite flatness to permit long-term alignment at low Reynolds numbers, as postulated by Borker *et al.* (2018).

The influence of inertia on the period of rotation is addressed in figure 6, where the experimentally measured period of rotation, T, is plotted against the particle Reynolds number, Re_p. The period is normalised by the Jeffery period, $T_J = 2\pi(r_{eq} + 1/r_{eq})/\dot{\gamma}$, using the equivalent aspect ratio r_{eq} inferred from the data of figure 5 at low Re_p. For $Re_p < 0.8$, inertia has a negligible effect on the period of rotation, which remains equal

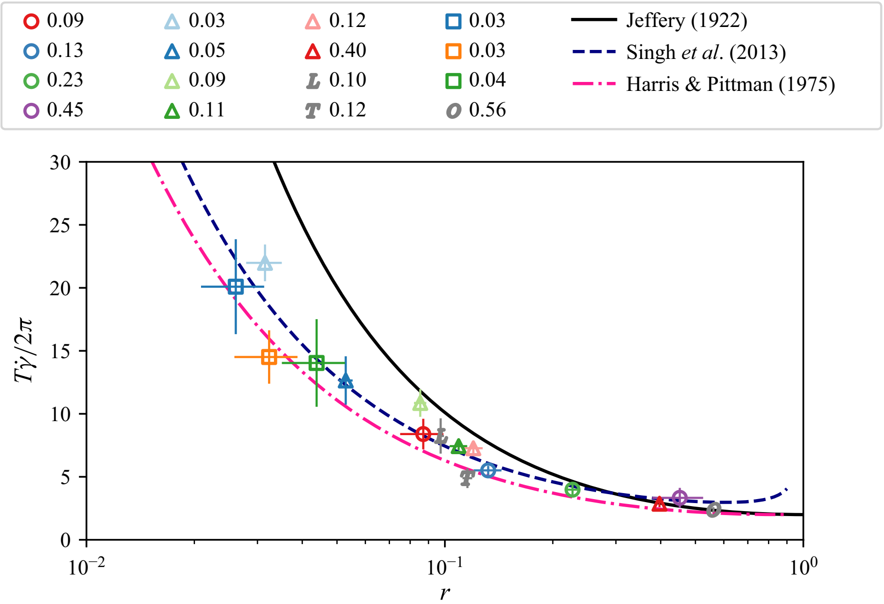

Figure 5. Period of rotation, T, of the flat bodies of revolution against the particle aspect ratio r. The period is made dimensionless using the shear rate $\dot{\gamma}$ and normalised by a factor 2π. The experimental values are displayed as coloured circles (rings with circular-shaped cross-section), triangles (rings with triangular-shaped cross-section) and squares (disks). The special rings with L- and T-shaped cross-section as well as the oblate ellipsoid are displayed with the letters $\boldsymbol{L}$, $\boldsymbol{T}$ and $\boldsymbol{O}$. Each point is the average over all the available experiments for small particle Reynolds numbers ($Re_p \lesssim 0.5$). The theory of Jeffery (1922), the semi-empirical correlation of Singh *et al.* (2013) and the empirical expression of Harris & Pittman (1975) are displayed as a solid black line, a dashed blue line and a dash-dotted pink line, respectively. See the Supplementary material for the directory of the figure including the data and the Jupyter Notebook (https://www.cambridge.org/S0022112025104217/JFM-Notebooks/files/figure_5/Figure_5.ipynb).

to the Jeffery period, T_J. As $Re_p \gtrsim 1$, the period exhibits a noticeable increase and, in the case of flat disks and rings with triangular cross-sections, may even reach infinity.

3.2. *Dynamics*

Having previously examined the influence of inertia on the period in figure 6, we now turn our attention to the effect of inertia on the global dynamics of the flat bodies. Figures 7, 8 and 9 display the three components of $\boldsymbol{n}$ in the flow (n_1), gradient (n_2) and vorticity (n_3) directions against the dimensionless time, $t\dot{\gamma}$. To facilitate clarity of presentation, we have chosen to focus the discussion on a subset of four runs for a typical circular ring (i.e. a ring with circular-shaped cross-section), triangular ring (i.e. a ring with triangular-shaped cross-section) and disk at small $Re_p \lesssim 1$ and at larger $Re_p \gtrsim 1$. We also compare our results with the theory of Jeffery (1922) and the asymptotic theories of Einarsson *et al.* (2015*b*) and Dabade *et al.* (2016). It is important to stress that, although the theories consider an unbounded system, there is some degree of confinement in the experiments ($\kappa \approx 0.2{-}0.7$) which may influence the dynamical behaviours as outlined by Rosén *et al.* (2015*a*). Moreover, the asymptotic theories of Einarsson *et al.* (2015*b*) and Dabade *et al.* (2016) are strictly valid only for $Re_p \ll 1$. It is therefore not possible to expect these theories to accurately describe the dynamics at $Re_p \gtrsim 1$, as also discussed by Rosén *et al.* (2015*a*).

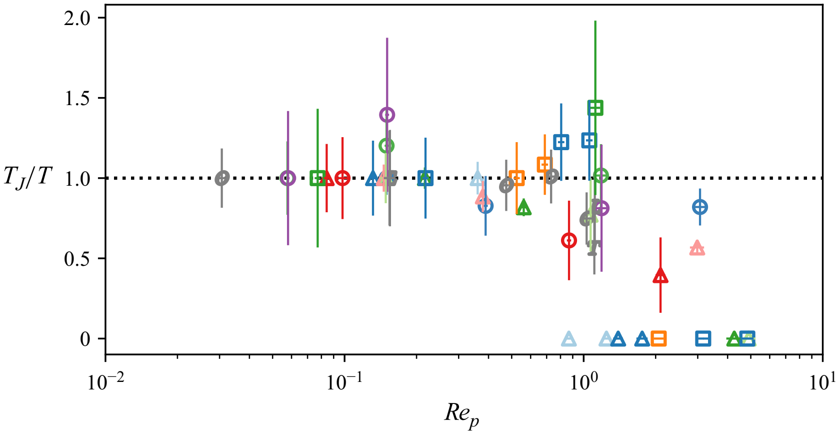

Figure 6. Inverse of the experimentally measured period of rotation T normalised by the Jeffery period, $T_J = 2\pi(r_{eq} + 1/r_{eq})/\dot{\gamma}$, against the particle Reynolds number, Re_p. The data symbols are identical to those in figure 5. Each point is the average over at least three experiments. The Jeffery period is calculated at the lowest particle Reynolds number for each particle, corresponding to the dotted black line within this normalisation. See the Supplementary material for the directory of the figure including the data and the Jupyter Notebook (https://www.cambridge.org/S0022112025104217/JFM-Notebooks/files/figure_6/Figure_6.ipynb).

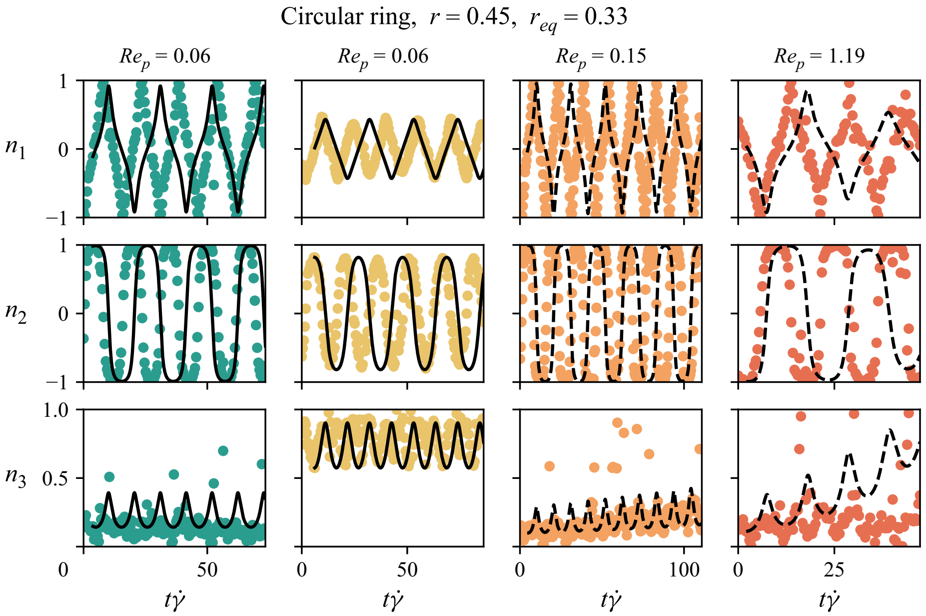

Figure 7. Evolution of the components of the orientation vector $\boldsymbol{n}$, displayed as vertically aligned panels, against the dimensionless time $t\dot{\gamma}$ for the circular ring R05 with aspect ratio $r = 0.45$ at $Re_p = 0.06$, $Re_p = 0.06$, $Re_p = 0.15$ and $Re_p = 1.19$ (from left to right). The two cases at $Re_p = 0.06$ correspond to different initial orientations, leading to different Jeffery orbits. Comparison with the model of Jeffery (1922) and of Einarsson *et al.* (2015*b*) are also given as black solid lines and black dashed lines, respectively. See Supplementary movies 2–4 for animations and the Jupyter Notebook (https://www.cambridge.org/S0022112025104217/JFM-Notebooks/files/figure_7/Figure_7.ipynb) of the figure including the data.

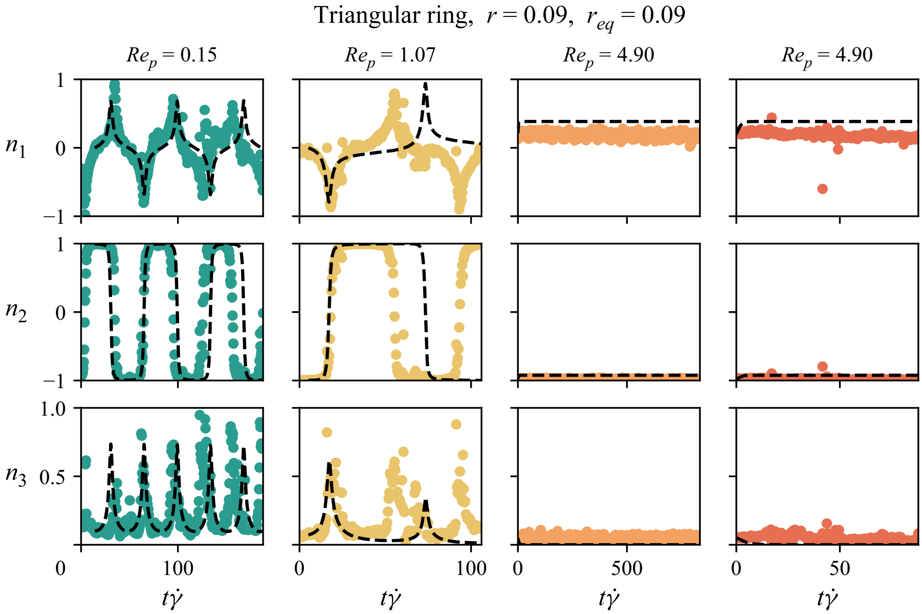

Figure 8. Evolution of the components of the orientation vector $\boldsymbol{n}$, displayed as vertically aligned panels, against the dimensionless time $t\dot{\gamma}$ for the triangular ring TR008 with aspect ratio $r = 0.09$ at $Re_p = 0.15$, $Re_p = 1.07$, $Re_p = 4.90$ and $Re_p = 4.90$ (from left to right). The two cases at $Re_p = 4.90$ demonstrate the systematic alignment of the particle in the plane of shear. Comparison with the model of Einarsson *et al.* (2015*b*) is also given as black dashed lines. See Supplementary movies 5–7 for animations and the Jupyter Notebook (https://www.cambridge.org/S0022112025104217/JFM-Notebooks/files/figure_8/Figure_8.ipynb) of the figure including the data.

We start by examining the influence of inertia on the dynamics of the circular ring with aspect ratio $r = 0.45$. At very small $Re_p = 0.06$, the ring approximately follows a Jeffery orbit with no significant drift between the successive rotations. At larger $Re_p = 0.15$ and $Re_p = 1.19$, the ring appears to remain in the tumbling orbit in the plane of shear during several periods of rotation. At $Re_p = 0.15$, the ring dynamics are well described by the asymptotic theory of Einarsson *et al.* (2015*b*) and a slow drift toward the spinning orbit may be discernable. At $Re_p = 1.19$, the ring is predicted to drift into a spinning orbit, but in the experiments, the ring remains in a tumbling orbit. As observed in experiments on oblate spheroids and disks (Di Giusto *et al.* 2024), the bifurcation towards a single stable spinning orbit above a critical aspect ratio of approximately 0.14, predicted by asymptotic theory of Einarsson *et al.* (2015*b*) as well as by the numerical simulations of Rosén *et al.* (2015*a*) at $Re_p = 1{-}5$, does not appear to be clearly observed for a circular ring. However, since inertial effects also depend on the detailed particle geometry, there is no fundamental reason why the critical aspect ratio for rings should be the same as that of spheroids, even with the same equivalent aspect ratio. As previously noted, these theories are strictly valid for $Re_p \ll 1$. It may be that discerning a clear bifurcation towards the spinning orbit in the experiments may necessitate a considerably longer observational timeframe, i.e. over more than 10 rotational periods, which is challenging to achieve experimentally.

We then consider the triangular ring with aspect ratio $r = 0.09$ in figure 8. At small $Re_p = 0.15$, a drifting behaviour is observed in agreement with the asymptotic theory of Einarsson *et al.* (2015*b*). For larger $Re_p = 1.07$, the asymptotic theories predict a slightly faster drift, which is expected since these theories are strictly valid only for $Re_p \ll 1$.

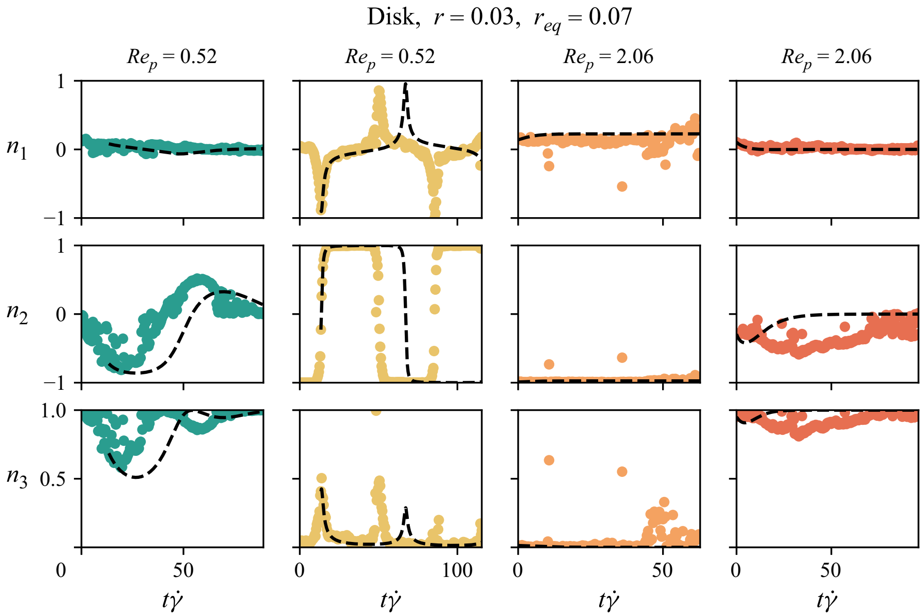

Figure 9. Evolution of the components of the orientation vector $\boldsymbol{n}$, displayed as vertically aligned panels, against the dimensionless time $t\dot{\gamma}$ for the disk D003 with aspect ratio $r = 0.03$ at $Re_p = 0.52$, $Re_p = 0.52$, $Re_p = 2.06$ and $Re_p = 2.06$ (from left to right). Comparison with the model of Einarsson *et al.* (2015*b*) is also given as black dashed lines. The two cases at $Re_p = 0.52$ correspond to different initial orientations, resulting in an inertial drift towards the spinning (first column) and tumbling (second column) limiting cycles. The two cases at $Re_p = 2.06$ correspond to different initial orientations, determining an alignment of the particle in the plane of shear (third column) or in the vorticity direction (fourth column). See Supplementary movies 8–9 for animations and the Jupyter Notebook (https://www.cambridge.org/S0022112025104217/JFM-Notebooks/files/figure_9/Figure_9.ipynb) of the figure including the data.

It is noteworthy that the period of rotation is observed to increase from $Re_p = 0.15$ to $Re_p = 1.07$. For even larger $Re_p = 4.09$, a permanent alignment in the plane of shear is observed.

Finally, we turn to the discussion of the disk D003 with aspect ratio $r = 0.03$ in figure 9. For the smallest $Re_p = 0.52$, the particle experiences a drift towards either a spinning or a tumbling orbit, contingent upon its initial orientation. The theory of Einarsson *et al.* (2015*a*) successfully predicts the existence of these two limiting orbits. For larger $Re_p = 2.06$, alignments with orientation either in the plane of shear or in the vorticity direction are observed.

3.3. *Bifurcations*

A summary of the dynamical behaviours exhibited by the circular and triangular rings as well as the disks can be found in the bifurcation map displayed in figure 10 which follows that proposed by Rosén *et al.* (2015*a*). The Re_p versus r_{eq} map shows whether the observed dynamics is rotational or aligning. Empty data symbols represent rotational dynamics and full data symbols represent aligning dynamics. The map depicts various bifurcation limits. It should be noted that the map provides a comprehensive representation of both oblate and prolate sides for the sake of completeness.

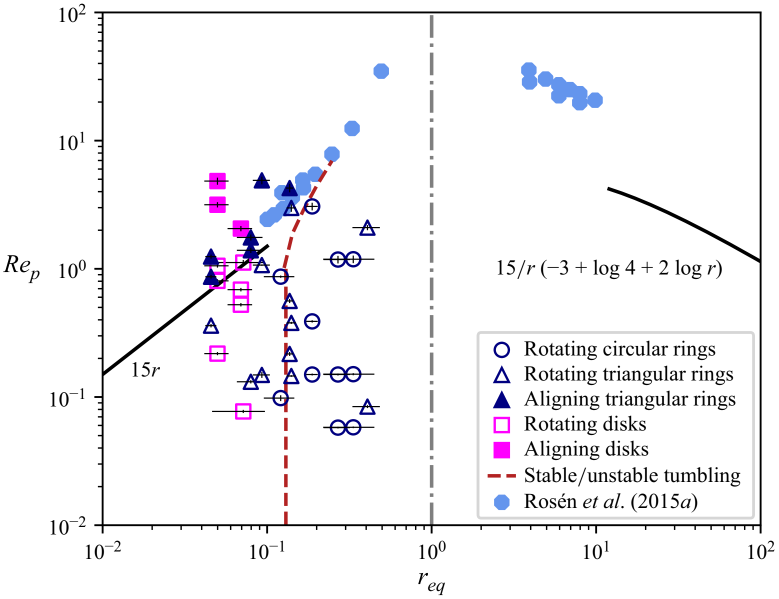

Figure 10. Particle Reynolds number, Re_p, against the equivalent particle aspect ratio, r_{eq}. The experiments are displayed as coloured circles (rings with circular-shaped cross-section), triangles (rings with triangular-shaped cross-section) and squares (disks), which are empty (or full) when rotational (or aligning) dynamics is observed. Each point is the average over at least three experiments. The equivalent particle aspect ratio is calculated at the lowest particle Reynolds number for each particle. The bifurcations between stable tumbling and stable fixed orientation in the slender oblate and prolate limits derived by Rosén *et al.* (2015*a*) are shown as black solid lines, while the bifurcation between stable and unstable tumbling given by Einarsson *et al.* (2015*b*) and Dabade *et al.* (2016), and extended to the small inertial regime by Rosén *et al.* (2015*a*), is drawn as a brown dashed line. The limits between tumbling and stable orientation given by the lattice Boltzmann as well as the steady-state simulations of Rosén *et al.* (2015*a*) are also displayed as solid cyan octagons. See the Supplementary material for the directory of the figure including the data and the Jupyter Notebook (https://www.cambridge.org/S0022112025104217/JFM-Notebooks/files/figure_10/Figure_10.ipynb).

The predicted bifurcation from stable to unstable tumbling is indicated by the brown dashed line. This bifurcation was predicted to occur at a critical aspect ratio of 0.137 in the asymptotic theories (Einarsson *et al.* 2015*b*; Dabade *et al.* 2016). This bifurcation limit was extended in the time-resolved lattice Boltzmann simulations of Rosén *et al.* (2015*a*) and shown to survive up to $Re_p = 5$, even with a confinement of $\kappa = 0.2$. This bifurcation was unexpectedly not observed in the previous experiments of Di Giusto *et al.* (2024) having similar confinement and is still not clearly observed in the present experiments. As previously mentioned in § 3.2, it is possible that the transition from a tumbling to a spinning orbit may require a significantly longer observational timeframe.

The bifurcation from tumbling in the flow-shear plane to a stable fixed orientation is given by the solid lines in the oblate and prolate asymptotic limits as predicted by the asymptotic theory (Rosén *et al.* 2015*a*). Bifurcations to a fixed point, as observed in the lattice Boltzmann as well as steady-state simulations, are also indicated by solid cyan octagons. The agreement between the predictions of the asymptotic theory and the simulations is only qualitative, as the theory is only valid for $Re_p \ll 1$. The present experimental bifurcation limit for disks and rings appears to be in good agreement with the numerical simulations carried out for spheroids. This further suggests that the Re_p versus r_{eq} bifurcation map is the most appropriate description for these systems beyond spheroids.

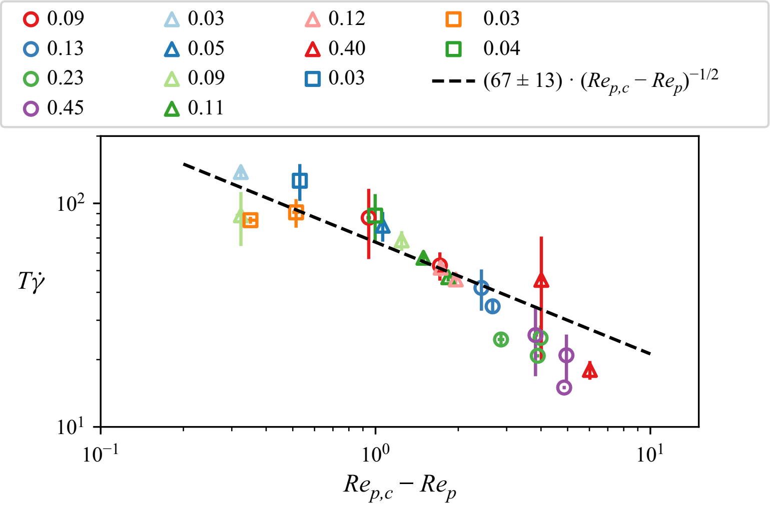

Figure 11. Dimensionless period, $T\dot{\gamma}$, versus the distance to the bifurcation to a fixed orientation, $Re_{p,c} - Re_p$. The dashed line is the best fit of the experimental data to the scaling law $(Re_{p,c} - Re_p)^{-1/2}$ using the critical particle Reynolds number predicted by the asymptotic theory, $Re_{p,c} = 15\,r_{eq}$ (Rosén *et al.* 2015*a*). The data symbols are identical to those in figure 5. See the Supplementary material for the directory of the figure including the data and the Jupyter Notebook (https://www.cambridge.org/S0022112025104217/JFM-Notebooks/files/figure_11/Figure_11.ipynb).

We now examine the critical behaviour of the period below the bifurcation, as illustrated in figure 11. The period, which has been normalised by the shear rate, $T\dot{\gamma}$, is plotted against the distance to the bifurcation towards a fixed orientation, $Re_{p,c} - Re_p$. It tends to infinity as $(Re_{p,c} - Re_p)^{-1/2}$ using the critical particle Reynolds number predicted by the asymptotic theory (Rosén *et al.* 2015*a*), $Re_{p,c} = 15\,r_{eq}$ (as $r_{eq} \rightarrow 0$), which is indicated in figure 10. This result is in agreement with the prediction of Ding & Aidun (2000) and the experiments of Zettner & Yoda (2001). The fitting of the data yields a prefactor of 67 ± 13. The experimental data deviate from this scaling law when the distance from the threshold becomes too large, i.e. $Re_{p,c} - Re_p \gtrsim 3$, as can be expected from a critical behaviour.

Figure 12 compares the behaviour of the alignment angle in the flow-shear plane, ϕ_a, with the aspect ratio, r_{eq}, above the bifurcation with the prediction of the asymptotic theory (Rosén *et al.* 2015a). This theory predicts that the flat body aligns in the flow-shear plane at the azimuthal angle $\phi_a = \pi/2 + r_{eq} + (30\,r_{eq})^{1/2}(Re_{p,c} - Re_p)^{1/2}/15$ with $Re_{p,c} = 15\,r_{eq}$ as $r_{eq} \rightarrow 0$. The theoretical predictions have been calculated using the experimental, r_{eq}, and experimental distance to the bifurcation, $Re_{p,c} - Re_p$. The experimental data qualitatively follow the predictions. It is clear that as the flatness increases, the orientation angle becomes more perpendicular to the flow direction.

4. Concluding remarks

The rotational dynamics of neutrally buoyant flat bodies of revolution (spheroids, disks and rings with different cross-sectional shapes) have been examined in shear flows. A custom-built shearing cell and deep learning methods have been used to obtain direct measurements of the orientation and period of rotation of these bodies.

At low particle Reynolds numbers, these bodies rotate with the Jeffery period, exhibiting an equivalent aspect ratio that is in good agreement with the predictions of Singh *et al.* (2013) for rings with circular or triangular cross-sections, and with the correlations of

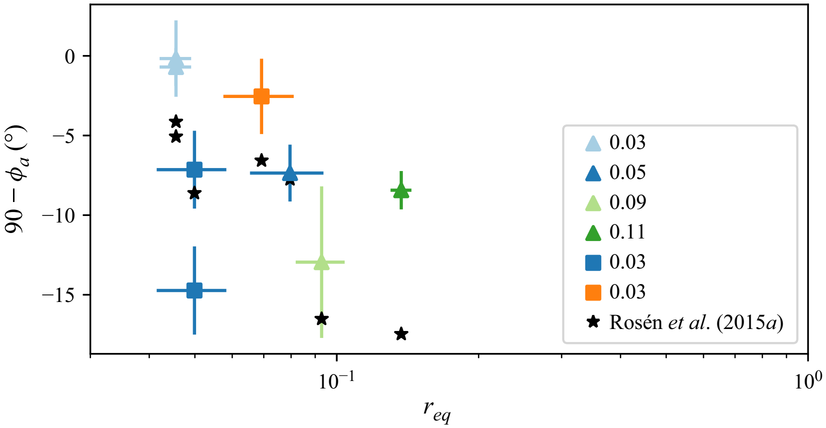

Figure 12. Alignment angle in the flow shear plane, ϕ_a, versus the equivalent aspect ratio, r_{eq}. Comparison with the prediction of the asymptotic theory, $\phi_a = \pi/2 + r_{eq} + (30\, r_{eq})^{1/2}(Re_{p,c} - Re_p)^{1/2}/15$ with $Re_{p,c} = 15\, r_{eq}$ as $r_{eq} \to 0$ (Rosén *et al.* 2015*a*). See the Supplementary material for the directory of the figure including the data and the Jupyter Notebook (https://www.cambridge.org/S0022112025104217/JFM-Notebooks/files/figure_12/Figure_12.ipynb).

Harris & Pittman (1975) for rings with L- and T-shaped cross-sections, oblate ellipsoids and disks. In contrast to the expectations set forth by Borker *et al.* (2018), no permanent alignment has been observed for flat rings with triangular cross-sections in the Stokes regime, even for the lowest aspect ratio of $r \approx 0.03$.

When inertia is augmented, the rings are observed to migrate across Jeffery orbits towards two attracting limiting orbits, namely the spinning orbit or the tumbling orbit, contingent upon their initial orientation, as previously observed for oblate spheroids and disks (Di Giusto *et al.* 2024). This is consistent with the theories of Einarsson *et al.* (2015*b*) and Dabade *et al.* (2016). However, as previously seen for oblate spheroids and disks (Di Giusto *et al.* 2024), a clear bifurcation between stable and unstable tumbling is not observed in contrast to the predictions of the asymptotic theories (Einarsson *et al.* 2015*b*; Dabade *et al.* 2016) and simulations (Rosén *et al.* 2015*a*). This unexpected result may be attributed to the fact that the transition from a tumbling to a spinning orbit may necessitate a considerably longer observational timeframe than that which can be practically achieved in laboratory experiments. Also, an influence of the confinement ratio cannot be entirely ruled out, and further investigation will be necessary to clarify this phenomenon. Overall, there is a need for a more thorough explanation of the discrepancy between experiments and the predictions of theory and simulations.

As the inertia is further increased, the period of rotation increases. For $Re_p \approx O(1)$, a sharp bifurcation to permanent alignment (with orientation either in the flow-shear plane or along the vorticity direction) is even observed for flat rings of triangular cross-sectional shape and flat disks. Below this bifurcation, the period is observed to approach infinity as a power law of the distance to the transition with an exponent of $-1/2$, in agreement with previous numerical predictions (Ding & Aidun 2000; Rosén *et al.* 2014, 2015*a*) and experimental observations (Zettner & Yoda 2001). Above this bifurcation, flat rings of triangular cross-sectional shape and flat disks align in the flow-shear plane at an orientation azimuthal angle that becomes more perpendicular to the flow direction with increasing flatness, in qualitative agreement with the prediction of the asymptotic theory (Rosén *et al.* 2015*a*).

Supplementary movies. Supplementary movies and Computational Notebook files are available at https://doi.org/10.1017/jfm.2025.10421. Computational Notebooks can also be found online at https://www.cambridge.org/S0022112025104217/JFM-Notebooks.

Acknowledgements. The authors would like to express their gratitude to J.E. Butler for introducing them to this problem and to C.K. Aidun for providing valuable insights on the bifurcation to a stable orientation. This work was partly carried out under the auspices of the ANR project 'Mechanics of bioinspired fibrous material' (ANR-21-CE30-019-01).

Funding. D.D.G. acknowledges the Universitá Italo-Francese, Bando Vinci 2021, cap. 2, progetto C2-257 'Fibre flessibili in flusso turbolento ad elevato numero di Reynolds'; for the generous funding.

Declaration of interests. The authors report no conflict of interest.

Appendix A. Data set generation

Although not available in the literature, labelled datasets of oriented axisymmetric particles can be conveniently generated through virtual modelling and rendering practices described here. During fabrication, each particle is modelled as a mesh of connected triangles in Blender Community (2018). This software also offers a powerful framework to render objects in 3-D scenes, conveniently managed through Python scripting. Therefore, a virtual scene with two perpendicular cameras is configured in Blender, recreating the disposition of the experimental set-up. Under ideal lighting conditions, the '.stl' file corresponding to the given particle is placed in the centre of the camera fields, with a square field of view of size $4a \times 4a$ at a resolution of 100×100 pixels. A Python script then iterates over 80×40 randomly sampled values of azimuth ϕ and polar θ angles, uniformly distributed to cover the entire range of the polar coordinates (np.random.uniform function of the numpy Python package). At each iteration, the particle is oriented according to the current polar coordinates and randomly shifted around the origin of the scene before the two cameras render one image each, corresponding to the top and side views of the experimental set-up, and labelled with the three components of the current particle orientation vector $\boldsymbol{n}$. This procedure results in a synthetic data set of 3200 pairs of perpendicular images of a given particle labelled with its orientation. The data set encompasses the full range of possible orientations and is applicable to cases where the particle is not perfectly centred in the camera field. See the Supplementary material for the Python script and the Blender scene files.

Appendix B. Training

The model deployed in this study adapts the LeNet-5 architecture (LeCun *et al.* 1998) to a two-stream format, which is necessary to jointly process the videos synchronously recorded by the top and side cameras. It is advantageous to develop a separate model for each particle, but fine-tuning among the same shapes (disc, spheroid, circular ring and triangular ring) speeds-up the convergence during training. Each neural network is trained using small-batching for approximately 100 epochs until a residual error of less than 10 % over the training data is achieved. The chosen optimiser is 'Adam' with a default learning rate of 0.001. The training procedure takes a limited amount of time, of the order of a few minutes. An 80–20 % splitting between train and test sets is applied to each particle synthetic dataset. As displayed in figure 13(*a*), both train and test residual error curves converge during the training, highlighting the good generalisation of the model over the unseen test data, very important for the accurate reconstruction of the experimental orbits. The histogram of the final errors over train and test sets is also displayed in figure 13(*b*), confirming the quality of the final predictions. These results are

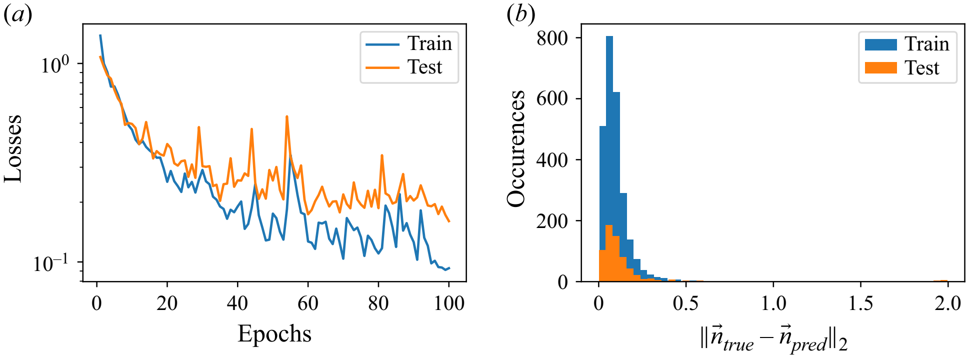

Figure 13. Evaluation of the model performance during training on the ELL06 synthetic particle dataset. (*a*) Train and test loss curves against the number of epochs. (*b*) Histogram of the final norm-2 between true and estimated values of the particle orientation vector $\boldsymbol{n}$ for both train and test sets. See the Supplementary material for the directory of the figure including the data and the Jupyter Notebook (https://www.cambridge.org/S0022112025104217/JFM-Notebooks/files/figure_13/Figure_13.ipynb).

obtained by applying a L_2 regularisation to the weights of the convolutional layers during the training to prevent the model from overfitting over the train set. The regularisation weight is set to 0.001. The inference of an experiment is completed in less than a second. The resolution of the experimental frames is adjusted by nearest interpolation to match that of the synthetic images, over which the models are trained. We examine the sensitivity to the resolution of the synthetic images, but find no significant improvement when the resolution is increased by a factor of 4 or 16. The influence of the size of the dataset on the accuracy of the measurement was evaluated, with the finding that a higher number of images typically leads to smoother predictions. Finally, the possibility of using only one camera for the measurements was tested with encouraging results. This opens up interesting measurement perspectives for particularly challenging experimental scenarios. Overall, we have proposed an original method for measuring the orientation of fore–aft axisymmetric and asymmetric particles suspended in viscous shear flows using deep learning. The method is highly generalisable to any scene that can be reproduced in the proposed context, and therefore has applications beyond the field of fluid mechanics. For this reason, all scripts and a sample of the training data are available at the repository https://github.com/ddg93/LeRing_JFM.

REFERENCES

BOJARSKI, M. *et al.* 2016 End-to-end learning for self-driving cars. arXiv:1604.07316.

BORKER, N.S., STROOCK, A.D. & KOCH, D.L. 2018 Controlling rotation and migration of rings in a simple shear flow through geometric modifications. *J. Fluid Mech.* **840**, 379–407.

BRADSKI, G. 2000 *The openCV library*. Dr. Dobb's Journal of Software Tools.

BRETHERTON, F.P. 1962 The motion of rigid particles in a shear flow at low Reynolds number. *J. Fluid Mech.* **14** (2), 284–304.

CAI, S., ZHOU, S., XU, C. & GAO, Q. 2019 Dense motion estimation of particle images via a convolutional neural network. *Exp. Fluids* **60** (4), 1–16.

Community, Blender Online 2018 *Blender – a 3-D Modelling and Rendering Package*. Blender Foundation, Stichting Blender Foundation.

DABADE, V., MARATH, N.K. & SUBRAMANIAN, G. 2016 The effect of inertia on the orientation dynamics of anisotropic particles in simple shear flow. *J. Fluid Mech.* **791**, 631–703.

DI GIUSTO, D., BERGOUGNOUX, L., MARCHIOLI, C. & GUAZZELLI, É. 2024 Influence of small inertia on jeffery orbits. *J. Fluid Mech.*. **979**, A42.

DING, E.-J. & AIDUN, C.K. 2000 The dynamics and scaling law for particles suspended in shear flow with inertia. *J. Fluid Mech.* **423**, 317–344.

EINARSSON, J., CANDELIER, F., LUNDELL, F., ANGILELLA, J.R. & MEHLIG, B. 2015*a* Effect of weak fluid inertia upon Jeffery orbits. *Phys. Rev. E* **91** (4), 041002.

EINARSSON, J., CANDELIER, F., LUNDELL, F., ANGILELLA, J.R. & MEHLIG, B. 2015*b* Rotation of a spheroid in a simple shear at small Reynolds number. *Phys. Fluids* **27** (6), 063301.

FUKUSHIMA, K. 1980 Neocognitron: a self-organizing neural network model for a mechanism of pattern recognition unaffected by shift in position. *Biol. Cybern.* **36** (4), 193–202.

HARRIS, J.B. & PITTMAN, J.F.T. 1975 Equivalent ellipsoidal axis ratios of slender rod-like particles. *J. Colloid Interface Sci.* **50** (2), 280–282.

HUBEL, D.H. & WIESEL, T.N. 1959 Receptive fields of single neurones in the cat's striate cortex. *J. Physiol.* **148** (3), 574–591.

HUBEL, D.H. & WIESEL, T.N. 1968 Receptive fields and functional architecture of monkey striate cortex. *J. Physiol.* **195** (1), 215–243.

JEFFERY, G.B. 1922 The rotation of two circular cylinders in a viscous fluid. *Proc. R. Soc. Lond. A* **101** (709), 169–174.

KRIZHEVSKY, A., SUTSKEVER, I. & HINTON, G.E. 2012 Imagenet classification with deep convolutional neural networks. *Adv. Neur. Inf. Proc. Syst.* **25**, 1–9.

LECUN, Y., BOTTOU, L., BENGIO, Y. & HAFFNER, P. 1998 Gradient-based learning applied to document recognition. *Proc. IEEE* **86** (11), 2278–2324.

MARATH, N.K. & SUBRAMANIAN, G. 2017 The effect of inertia on the time period of rotation of an anisotropic particle in simple shear flow. *J. Fluid Mech.* **830**, 165–210.

MARATH, N.K. & SUBRAMANIAN, G. 2018 The inertial orientation dynamics of anisotropic particles in planar linear flows. *J. Fluid Mech.* **844**, 357–402.

NEWBY, J.M., SCHAEFER, A.M., LEE, P.T., FOREST, M.G. & LAI, S.K. 2018 Convolutional neural networks automate detection for tracking of submicron-scale particles in 2-D and 3-D. *Proc. Natl Acad. Sci.* **115** (36), 9026–9031.

REDMON, J., DIVVALA, S., GIRSHICK, R. & FARHADI, A. 2016 You only look once: unified, real-time object detection. In *Proceedings of the IEEE Conference on Computer Vision and Pattern Recognition*, pp. 779–788.

ROSÉN, T., EINARSSON, J., NORDMARK, A., AIDUN, C.K., LUNDELL, F. & MEHLIG, B. 2015*a* Numerical analysis of the angular motion of a neutrally buoyant spheroid in shear flow at small Reynolds numbers. *Phys. Rev. E* **92** (6), 063022.

ROSÉN, T., LUNDELL, F. & AIDUN, C.K. 2014 Effect of fluid inertia on the dynamics and scaling of neutrally buoyant particles in shear flow. *J. Fluid Mech.* **738**, 563–590.

ROSÉN, T., DO-QUANG, M., AIDUN, C.K. & LUNDELL, F. 2015*b* The dynamical states of a prolate spheroidal particle suspended in shear flow as a consequence of particle and fluid inertia. *J. Fluid Mech.* **771**, 115–158.

SINGH, V., KOCH, D.L. & STROOCK, A.D. 2013 Rigid ring-shaped particles that align in simple shear flow. *J. Fluid Mech.* **722**, 121–158.

SUBRAMANIAN, G. & KOCH, D.L. 2005 Inertial effects on fibre motion in simple shear flow. *J. Fluid Mech.* **535**, 383–414.

SUBRAMANIAN, G. & KOCH, D.L. 2006 Inertial effects on the orientation of nearly spherical particles in simple shear flow. *J. Fluid Mech.* **557**, 257–296.

SZEGEDY, C., LIU, W., JIA, Y., SERMANET, P., REED, S., ANGUELOV, D., ERHAN, D., VANHOUCKE, V. & RABINOVICH, A. 2015 Going deeper with convolutions. In *Proceedings of the IEEE Conference on Computer Vision and Pattern Recognition*, pp. 1–9.

TAIGMAN, Y., YANG, M., RANZATO, M. & WOLF, L. 2014 Deepface: Closing the gap to human-level performance in face verification. In *Proceedings of IEEE Conference on Computer Vision and Pattern Recognition*, pp. 1701–1708.

ZETTNER, C.M. & YODA, M. 2001 Moderate-aspect-ratio elliptical cylinders in simple shear with inertia. *J. Fluid Mech.* **442**, 241–266.